Transition from an atomic to a molecular Bose–Einstein condensate

https://doi.org/10.1038/s41586-021-03443-0

Received: 6 July 2020

Accepted: 11 March 2021

Published online: 28 April 2021

Check for updates

Zhendong Zhang[1], Liangchao Chen[2], Kai-Xuan Yao[1] & Cheng Chin[1]✉

Molecular quantum gases (that is, ultracold and dense molecular gases) have many potential applications, including quantum control of chemical reactions, precision measurements, quantum simulation and quantum information processing[1–3]. For molecules, to reach the quantum regime usually requires efficient cooling at high densities, which is frequently hindered by fast inelastic collisions that heat and deplete the population of molecules[4,5]. Here we report the preparation of two-dimensional Bose–Einstein condensates (BECs) of spinning molecules by inducing pairing interactions in an atomic condensate near a *g*-wave Feshbach resonance[6]. The trap geometry and the low temperature of the molecules help to reduce inelastic loss, ensuring thermal equilibrium. From the equation-of-state measurement, we determine the molecular scattering length to be + 220(±30) Bohr radii (95% confidence interval). We also investigate the unpairing dynamics in the strong coupling regime and find that near the Feshbach resonance the dynamical timescale is consistent with the unitarity limit. Our work demonstrates the long-sought transition between atomic and molecular condensates, the bosonic analogue of the crossover from a BEC to a Bardeen–Cooper–Schrieffer (BCS) superfluid in a Fermi gas[7–9]. In addition, our experiment may shed light on condensed pairs with orbital angular momentum, where a novel anisotropic superfluid with non-zero surface current is predicted[10,11], such as the A phase of ^{3}He.

Because of their rich energy structure, cold molecules may enable advances in quantum engineering and quantum chemistry[1–3]; a wide variety of platforms have been developed to trap and cool the cold molecules[2]. The same rich energy structure, however, also causes complex reactive collisions that obstruct experimental attempts to cool molecules towards quantum degeneracy.

One successful strategy towards preparing molecular quantum gas is to begin with an atomic quantum gas, and then to pair the atoms into molecules[6]. A prominent example is the pairing of atoms in a two-component Fermi gas, which opens the door to exciting research on the crossover from a BEC to a BCS superfluid[12–14]. Recently, a degenerate Fermi gas of ground-state KRb molecules has been produced from quantum mixtures of Rb and K atoms[15]. In these examples, molecules gain collisional stability from Fermi statistics and the preparation of molecules in the lowest rovibrational state, respectively.

For more generic molecules with many open inelastic channels, inelastic collision rates are difficult to predict and experiments frequently report rates near the unitarity limit, which means that all possible scatterings result in loss[4,5]. The short lifetime hinders evaporative cooling towards quantum degeneracy.

Here we report the observation of BECs of Cs_2 molecules in a high vibrational and rotational state; see Fig. 1. The molecules are produced by pairing Bose-condensed caesium atoms in a two-dimensional, flat-bottomed trap near a narrow *g*-wave Feshbach resonance[16]. The trap geometry allows molecules to form at very low temperature and with low collision loss such that they emerge into the Berezinskii–Kosterlitz–Thouless (BKT) superfluid regime[17–19]. Our experiment thus enables us to investigate pairing and unpairing dynamics in a bosonic many-body system, described by the interaction Hamiltonian[7–9]

$$H_{\mathrm{int}} = g(\hat{a}_{\mathrm{m}}^{\dagger}\hat{a}\hat{a} + \hat{a}_{\mathrm{m}}\hat{a}^{\dagger}\hat{a}^{\dagger}),$$

where $\hat{a}_{\mathrm{m}}$ and $\hat{a}$ are the annihilation operators of a molecule and an atom, respectively, and g is the coupling constant. Pairing of bosons is expected on both sides of the Feshbach resonance and can lead to an Ising-like quantum phase transition[7–9]. Interestingly, in the molecular BEC phase, atoms and molecules are predicted to have BCS-like correlations[8].

Our experiment starts with a BEC of 6×10^4 caesium atoms in a uniform optical trap. The radial confinement on the x–y plane comes from a circular, flat-bottomed optical potential[20]. The sample is vertically confined with 1/e radius of 0.4 μm to a single site of an optical lattice with trap frequency $\omega_z = 2\pi \times 400$ Hz. The atomic scattering length is $127a_0$ at $B = 19.2$ G and the global chemical potential is $\mu_0 = h \times 365$ Hz, where $h = 2\pi\hbar$ is the Planck constant and a_0 is the Bohr radius. The initial state of the atoms is a BEC in the two-dimensional (2D) to three-dimensional (3D) crossover regime at temperature $T = 11(2)$ nK, well below the BEC critical temperature of 85 nK.

We create Cs_2 molecules by ramping the magnetic field across a closed-channel dominated Feshbach resonance at $B_0 = 19.87$ G (ref. [21]).

[1]James Franck Institute, Enrico Fermi Institute and Department of Physics, University of Chicago, Chicago, IL, USA. [2]State Key Laboratory of Quantum Optics and Quantum Optics Devices, Institute of Opto-Electronics, Shanxi University, Taiyuan, China. ✉e-mail: cchin@uchicago.edu

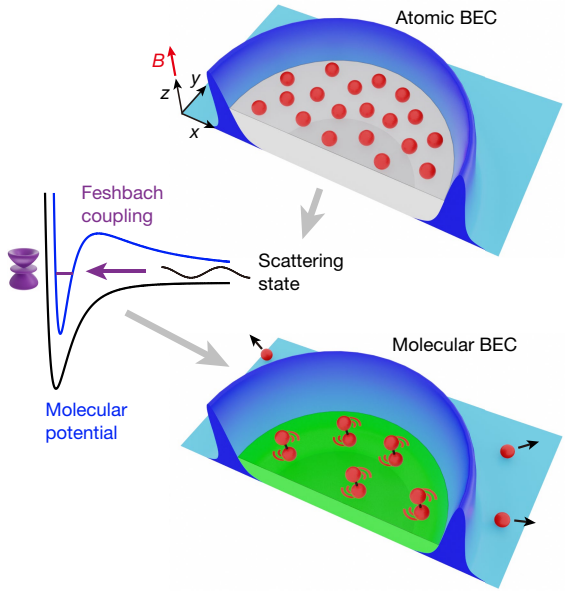

Fig. 1 | Production of *g*-wave molecular condensate. A uniform Cs BEC (grey) is initially confined in a 2D optical potential (blue). Caesium atoms (red circles) are paired into molecules through a narrow *g*-wave Feshbach resonance at magnetic field $B_0 = 19.87$ G. The molecules occupy a rotational state with orbital angular momentum $l = 4\hbar$ and its projection in the *z*-direction is $l_z = 2\hbar$. The molecules form a molecular BEC (green) in the same optical trap, while the remaining atoms are expelled from the trap.

This resonance has a small width $\Delta B = 11$ mG (ref. [22]) and couples two scattering atoms into a weakly bound molecule with a large orbital angular momentum $l = 4\hbar$ and projection along the magnetic field direction $l_z = 2\hbar$. The molecules are closed-channel dominated and chemically bound with the size given by the van der Waals length $R_{vdW} = 5.3$ nm for Cs (ref. [16]). This resonance is chosen owing to the superior collisional stability between the molecules. The molecules can be brought into other rotational states or superposition of rotational states by a time-dependent magnetic field[23].

The ramp is optimized to pair up to 15% of the atoms into molecules at the lowest achievable temperature. After the formation of the molecules, residual atoms are optically expelled from the trap and a magnetic field gradient is applied to levitate the molecules[21]. To detect the molecules, we dissociate them back to atoms by reversely ramping the field well above the resonance, and perform in situ imaging on the atoms; see Fig. 2a.

The molecules produced thus occupy the same trap volume as the atomic cloud. A slightly lower molecular density is observed at the trap centre owing to a weak magnetic field curvature of 21.5 G cm^{-2} on the *x*–*y* plane. The field curvature leads to a slightly deeper (by 1.1 nK) potential in the rim than in the centre for the molecules. The appearance of the ring structure in the molecular density profile (see Fig. 2a) suggests that the molecules are prepared at a temperature or chemical potential on the order of a few nanokelvin. The ring structure forms soon after passing the Feshbach resonance during the magnetic field ramp, which suggests that the equilibrium of molecules is reached by their fast interactions with atoms near the resonance (see Methods). This supports our equation-of-state measurements (below) of the molecular samples from their density profiles.

To determine the molecular temperature, we find the conventional time-of-flight method impractical because the molecules expand very slowly within their lifetime. Instead we measure the density profile by slowly raising a potential barrier at the trap centre over 10 ms and recording the density response; see Fig. 2b. With a high potential barrier, the molecules at the centre become thermal with the density response $\partial n/\partial\mu = n/k_B T$, where k_B is the Boltzmann constant. From fitting the data, we determine the molecular temperature to be 10(3) nK (the uncertainty in parentheses is the 95% confidence interval here and throughout unless otherwise stated). The low-temperature $k_B T < \hbar\omega_z$ also suggests that the molecules form a 2D gas.

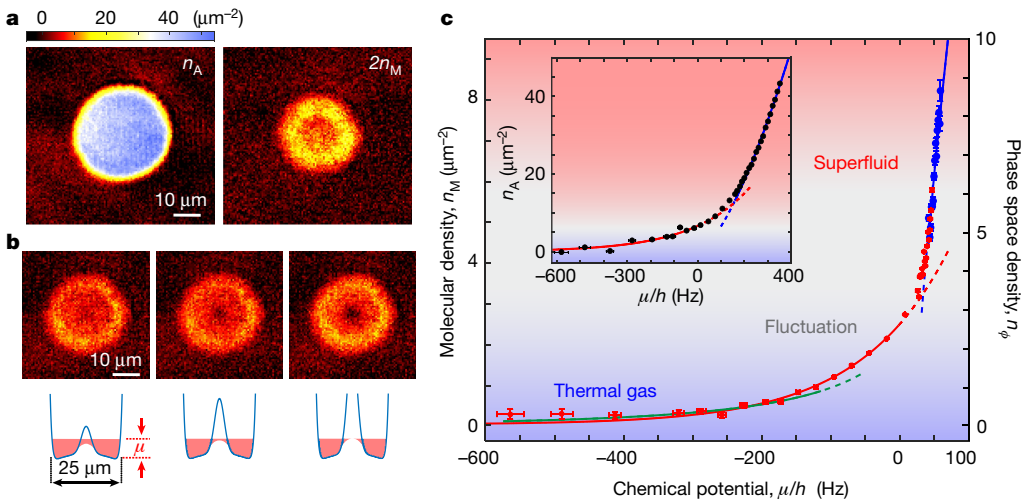

Fig. 2 | Equation of state of molecular gases. a, In situ images of atomic BEC (left) and molecular BEC (right) density profiles n_A and n_M, shown on the colour scale, both at $\mathbf{B} = 19.2$ G, in the dipole trap. Atoms are paired into molecules near the *g*-wave Feshbach resonance; see text. **b**, Molecular density response to optical potential. A circular repulsive barrier with a radius of 4 μm is raised at the centre of the trap with a barrier height of $h \times 83$ (left), $h \times 165$ (middle) and $h \times 330$ Hz (right). The molecular density response determines the equation of state for small and negative chemical potential. The total external potential is sketched below. The samples have a diameter of 25 μm. **c**, Equation of state of atomic and molecular BEC, $n(\mu)$, where μ is chemical potential. The 2D phase space density $n_\phi = n_M \lambda_{dB}^2$ of molecules is derived from the optical barrier (red) and density profile (blue) measurements (see Methods), where λ_{dB} is the molecular de Broglie wavelength. The background colour shows the 2D gas in the thermal ($n_\phi \leq 2$, blue), fluctuation ($2 < n_\phi < n_c$, grey) and BKT superfluid ($n_\phi > n_c$, red) regimes, where the superfluid critical phase space density is $n_c = 6.5$ (experimental) and 7.5 (theoretical); see text. The green and blue lines are fits in the thermal and superfluid regimes for a 2D Bose gas[26], respectively. The red line is a fit based on a classical gas. The inset shows identical measurement on atomic condensates with fits in the thermal (red) and BEC (blue) regimes. Data values represent the average and error bars represent one standard deviation of the mean, estimated from the statistical errors of 9–22 measurements.

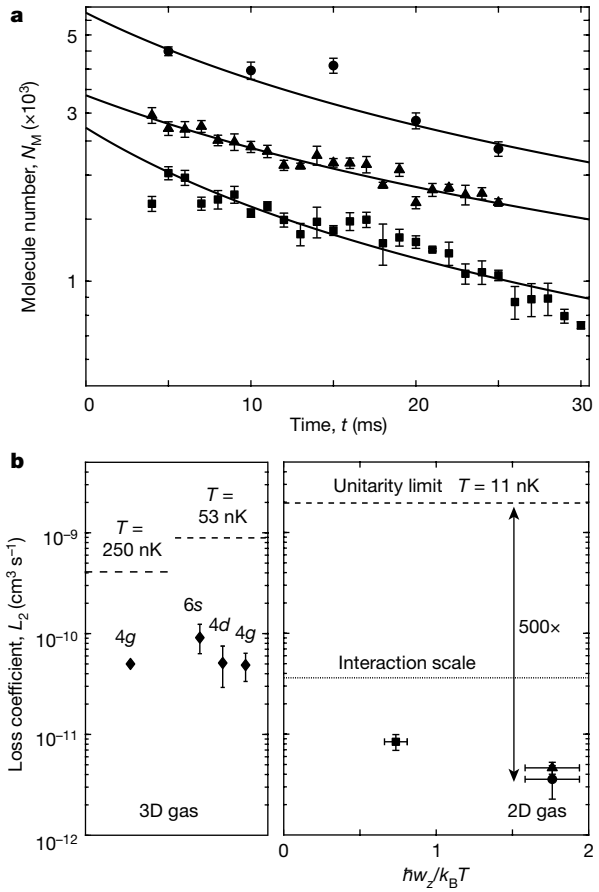

Fig. 3 | Stability of *g*-wave molecular condensate. a, Decay of total number of molecules with vertical trap frequency $\omega_z/2\pi = 400$ (circle and triangle symbols) and 167 Hz (square symbols) at 19.5 G. Data values and error bars are estimated as in Fig. 2 from 3–10 measurements. The solid lines are fits based on the two-body loss rate equation (see Methods). **b**, The extracted loss coefficients L_2 in this work (right panel) are compared with former measurements on 3D thermal gases of Cs_2 molecules in the 6*s*, 4*d* and 4*g* states (left panel)[29,30]. Permission to show the data is granted by the Innsbruck group. The data points in the right panel share the same symbols as in **a**. The error bars represent 95% confidence interval from the fits. The dashed lines indicate the unitarity limits of the two-body loss coefficients. The dotted line shows the interaction energy scale $\mu_0/\hbar n_{3D}$ for the circular data point at 10 ms in **a** with global chemical potential $\mu_0 = h \times 61$ Hz and mean 3D density $n_{3D} = 1.1 \times 10^{13}$ cm^{-3}.

To probe the phase of the molecules at high densities, we measure the equation of state $n(\mu, T)$ from their in situ density distribution[24]. Precise knowledge of the magnetic anti-trap potential is obtained from identical measurements with atomic condensates (see Methods). The molecular density is found to linearly increase with the local chemical potential, consistent with the mean-field expectation $\mu = \hbar^2 g_{2D} n_M/2m$, where $g_{2D} = 4\pi a_M \sqrt{2m\omega_z/\hbar}$ is the 2D coupling constant[25], n_M is the 2D molecular density, m is the atomic mass and a_M is the molecular scattering length. Fitting the data with the theoretical prediction including finite temperature contribution[26], we obtain a temperature of 11(1) nK, consistent with the optical barrier measurement.

We combine both measurements to determine the equation of state $n(\mu, T)$ of the molecular gas. In Fig. 2c, we present the 2D density n_M as a function of the local chemical potential μ. Notably, the transition from exponential to linear dependence on μ is the hallmark of the transition from the thermal gas to the superfluid phase. A global fit to the data shows excellent agreement with the theory in the thermal and superfluid limits (see Methods). From the fit, we determine the 2D coupling constant $g_{2D} = 0.19(3)$, the molecular scattering length $a_M = +220(30)a_0$, the peak phase space density $n_\phi \approx 9$ and the global chemical potential $\mu_0 = h \times 61(7)$ Hz. Repeated experiments in the range of 18.2 G < B < 19.5 G show that a_M is approximately constant. The peak phase space density exceeds the critical value for the BKT superfluid transition of $n_c = 6.5$ (experimental value)[19] and 7.5 (theoretical value)[27] at $g_{2D} = 0.19$. On the basis of our trap geometry and the interaction strength, we expect that molecules condense in the superfluid regime[28], and estimate that 30% to 50% of the molecules are in the superfluid phase.

We further investigate the lifetime of the molecules. By holding the molecular BEC in the dipole trap with an initial mean density of $n_{3D} \approx 1 \times 10^{13}$ cm^{-3}, the sample survives for more than 30 ms. Comparing samples with different densities and in different traps, we conclude that the decays are dominated by two-body collision loss (see Methods); see Fig. 3a. The average loss coefficient of $L_2 = 4 \times 10^{-12}$ cm^3 s^{-1} for molecules in the 2D trap with $\omega_z/2\pi = 400$ Hz is about ten times lower than previous measurements[29,30]; see Fig. 3b. It is also a factor of 500 below the unitarity limit $U_2 = (4h/2m)\langle k^{-1}\rangle = 2 \times 10^{-9}$ cm^3 s^{-1}, where $\langle k^{-1}\rangle$ is the thermal average of the reciprocal molecular scattering wavenumber k^{-1} (see Methods), and a factor of 10 below the interaction scale $\mu_0/\hbar n_{3D}$; see Fig. 3b.

The large suppression of inelastic collisions between the highly excited *g*-wave molecules is remarkable. The comparison in Fig. 3b suggests that the collision loss is suppressed at low temperatures and possibly in the 2D regime[31,32]. Since the unitarity limited loss scales as $T^{-1/2}$, the smaller loss at lower temperature suggests that a larger suppression relative to the unitarity limit can be obtained by reaching even lower temperatures. At 10 nK, the loss coefficient we observe is already at the same level as the ground-state fermionic molecules reported in refs. [33,34].

The observed lifetime of 30 ms is sufficient for many elastic scattering events between molecules, which occur at the timescale of $\hbar/\mu_0 = 2.7$ ms. Although the lifetime is insufficient to re-distribute molecules over the entire sample, thermal equilibrium in a (nearly) homogeneous system does not require global transport and can form by local interactions near the Feshbach resonance, where fast collisions between atoms and molecules occur (see Methods). It is remarkable that the temperatures measured at the trap centre and in the rim are in good agreement with the atomic BEC at 11(2) nK. Our observation suggests that molecules produced at all locations in the trap are in thermal equilibrium with the atoms. Since the atoms are in thermal equilibrium, the molecules thus prepared are in thermal equilibrium with each other.

The molecular superfluid thus enables the investigation of pairing and unpairing in a Bose condensate. A phase transition is expected when unpairing occurs in a molecular BEC[7,8]. Figure 4 presents our investigation into the unpairing dynamics. After forming the molecular condensate at $B = 19.4$ G, we ramp the magnetic field in 0.3 ms near and above the Feshbach resonance with a precision of 2 mG. We monitor the dissociation process by imaging the emerging atoms.

When the field is ramped high above the resonance, the molecules quickly and entirely dissociate. In particular, the dissociation rate follows Fermi's golden rule $\Gamma \propto E^{1/2}$, where $E = \Delta\mu(B - B_0)$ is the molecular energy above the continuum and $\Delta\mu = h \times 770$ kHz G^{-1} is the relative magnetic moment[30].

Near the Feshbach resonance the system enters the strong coupling regime and the measurement deviates from Fermi's golden rule. Here the measured dissociation energy $\hbar\gamma = \hbar \times 8$ ms$^{-1} = k_B \times 61$ nK (see Fig. 4b), is much greater than μ and T of the BEC and much smaller than the Feshbach resonance width $\Delta\mu\Delta B = k_B \times 410$ nK. The energy is, however, comparable to the universal Fermi energy scale for the molecules $E_F = (\hbar^2/4m)(6\pi^2 n_{3D})^{2/3} = k_B \times 63$ nK. This result suggests that the dissociation dynamics near the Feshbach resonance is unitarity-limited[35,36]. Finally, we observe about 40% of the molecules converted back to atoms, and attribute the missing 60% to inelastic collisions between atoms and molecules in the strong coupling regime.

To conclude, we have realized a BEC of highly excited, rotating molecules near a narrow Feshbach resonance. The molecules are sufficiently

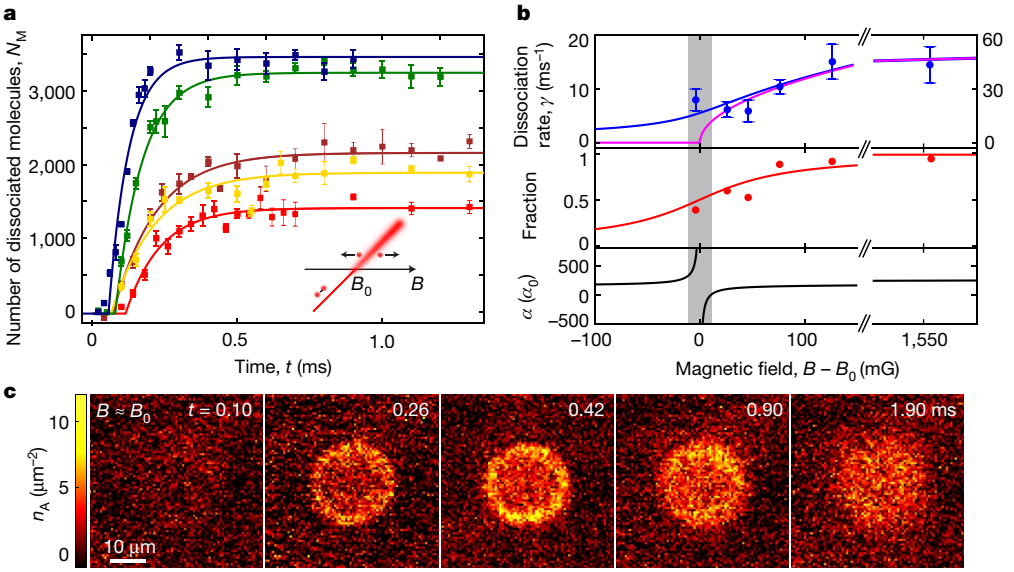

Fig. 4 | Unpairing dynamics in a molecular condensate near the *g*-wave Feshbach resonance at B_0 = 19.874 G. a, 5 ms after the formation of the molecular BEC with mean 3D density $n_{3D} = 9.7 \times 10^{12}$ cm^{-3}, we ramp the magnetic field back to 19.87 G (red), 19.90 G (brown), 19.92 G (yellow), 19.95 G (green) and 20.0 G (blue) and image the atoms from the dissociated molecules. Data values and error bars are estimated as in Fig. 2 from 3–8 measurements. The inset illustrates the unpairing process. **b**, The unpairing dissociation rate (upper panel) and unpaired fraction (middle panel) extracted from the solid-line fits in **a** are compared with the atomic *s*-wave scattering length a (lower panel). The error bars represent 95% confidence interval from the fits. The magenta and blue lines are empirical fits based on Fermi's golden rule with the bare and effective densities of states, respectively. The red line is an empirical fit (see Methods). The grey-shaded area represents the width of the *g*-wave Feshbach resonance. **c**, In situ images of unpaired molecules at B = 19.870(2) G near the Feshbach resonance.

stable at low temperatures to ensure local thermal equilibrium. Unpairing dynamics in molecular condensates is consistent with the universality hypothesis. Our system offers a platform with which to study the long-sought transition from an atomic BEC to a molecular BEC, and highlights the fundamental difference between Cooper pairing in a degenerate Fermi gas and bosonic pairing in a BEC.

Online content

Any methods, additional references, Nature Research reporting summaries, source data, extended data, supplementary information, acknowledgements, peer review information; details of author contributions and competing interests; and statements of data and code availability are available at https://doi.org/10.1038/s41586-021-03443-0.

1. Bohn, J. L., Rey, A. M. & Ye, J. Cold molecules: progress in quantum engineering of chemistry and quantum matter. *Science* **357**, 1002–1010 (2017).
2. Carr, L. D., DeMille, D., Krems, R. V. & Ye, J. Cold and ultracold molecules: science, technology and applications. *New J. Phys.* **11**, 055049 (2009).
3. Quéméner, G. & Julienne, P. S. Ultracold molecules under control! *Chem. Rev.* **112**, 4949–5011 (2012).
4. Mayle, M., Quéméner, G., Ruzic, B. P. & Bohn, J. L. Scattering of ultracold molecules in the highly resonant regime. *Phys. Rev. A* **87**, 012709 (2013).
5. Idziaszek, Z. & Julienne, P. S. Universal rate constants for reactive collisions of ultracold molecules. *Phys. Rev. Lett.* **104**, 113202 (2010).
6. Köhler, T., Góral, K. & Julienne, P. S. Production of cold molecules via magnetically tunable Feshbach resonances. *Rev. Mod. Phys.* **78**, 1311–1361 (2006).
7. Romans, M. W. J., Duine, R. A., Sachdev, S. & Stoof, H. T. C. Quantum phase transition in an atomic Bose gas with a Feshbach resonance. *Phys. Rev. Lett.* **93**, 020405 (2004).
8. Radzihovsky, L., Park, J. & Weichman, P. B. Superfluid transitions in bosonic atom-molecule mixtures near a Feshbach resonance. *Phys. Rev. Lett.* **92**, 160402 (2004).
9. Duine, R. A. & Stoof, H. T. C. Atom–molecule coherence in Bose gases. *Phys. Rep.* **396**, 115–195 (2004).
10. Anderson, P. W. & Morel, P. Generalized Bardeen–Cooper–Schrieffer states and the proposed low-temperature phase of liquid He^3. *Phys. Rev.* **123**, 1911 (1961).
11. Ho, T.-L. The Bose-Einstein condensate of g-wave molecules and its intrinsic angular momentum. Preprint at https://arxiv.org/abs/2101.05431 (2021).
12. Chen, Q., Stajic, J., Tan, S. & Levin, K. BCS-BEC crossover: from high temperature superconductors to ultracold superfluids. *Phys. Rep.* **412**, 1–88 (2005).
13. Giorgini, S., Pitaevskii, L. P. & Stringari, S. Theory of ultracold atomic Fermi gases. *Rev. Mod. Phys.* **80**, 1215–1274 (2008).
14. Timmermans, E., Furuya, K., Milonni, P. W. & Kerman, A. K. Prospect of creating a composite Fermi-Bose superfluid. *Phys. Lett. A* **285**, 228–233 (2001).
15. De Marco, L. et al. A degenerate Fermi gas of polar molecules. *Science* **363**, 853–856 (2019).
16. Chin, C., Grimm, R., Julienne, P. & Tiesinga, E. Feshbach resonances in ultracold gases. *Rev. Mod. Phys.* **82**, 1225–1286 (2010).
17. Krüger, P., Hadzibabic, Z. & Dalibard, J. Critical point of an interacting two-dimensional atomic Bose gas. *Phys. Rev. Lett.* **99**, 040402 (2007).
18. Tung, S., Lamporesi, G., Lobser, D., Xia, L. & Cornell, E. A. Observation of the presuperfluid regime in a two-dimensional Bose gas. *Phys. Rev. Lett.* **105**, 230408 (2010).
19. Hung, C.-L., Zhang, X., Gemelke, N. & Chin, C. Observation of scale invariance and universality in two-dimensional Bose gases. *Nature* **470**, 236–239 (2011).
20. Clark, L. W., Gaj, A., Feng, L. & Chin, C. Collective emission of matter-wave jets from driven Bose–Einstein condensates. *Nature* **551**, 356–359 (2017).
21. Herbig, J. et al. Preparation of a pure molecular quantum gas. *Science* **301**, 1510–1513 (2003).
22. Mark, M., Meinert, F., Lauber, K. & Nägerl, H.-C. Mott-insulator-aided detection of ultra-narrow Feshbach resonances. *SciPost Phys.* **5**, 055 (2018).
23. Mark, M. et al. "Stückelberg interferometry" with ultracold molecules. *Phys. Rev. Lett.* **99**, 113201 (2007).
24. Ho, T.-L. & Zhou, Q. Obtaining the phase diagram and thermodynamic quantities of bulk systems from the densities of trapped gases. *Nat. Phys.* **6**, 131–134 (2010).
25. Petrov, D. S. & Shlyapnikov, G. V. Interatomic collisions in a tightly confined Bose gas. *Phys. Rev. A* **64**, 012706 (2001).
26. Prokof'ev, N. & Svistunov, B. Two-dimensional weakly interacting Bose gas in the fluctuation region. *Phys. Rev. A* **66**, 043608 (2002).
27. Prokof'ev, N., Ruebenacker, O. & Svistunov, B. Critical point of a weakly interacting two-dimensional Bose gas. *Phys. Rev. Lett.* **87**, 270402 (2001).
28. Hadzibabic, Z. & Dalibard, J. Two-dimensional Bose fluids: an atomic physics perspective. *Riv. Nuovo Cim.* **34**, 389–434 (2011).
29. Ferlaino, F. et al. Collisions of ultracold trapped cesium Feshbach molecules. *Laser Phys.* **20**, 23–31 (2010).
30. Chin, C. et al. Observation of Feshbach-like resonances in collisions between ultracold molecules. *Phys. Rev. Lett.* **94**, 123201 (2005).
31. Idziaszek, Z., Jachymski, K. & Julienne, P. S. Reactive collisions in confined geometries. *New J. Phys.* **17**, 035007 (2015).
32. Micheli, A. et al. Universal rates for reactive ultracold polar molecules in reduced dimensions. *Phys. Rev. Lett.* **105**, 073202 (2010).
33. de Miranda, M. H. G. et al. Controlling the quantum stereodynamics of ultracold bimolecular reactions. *Nat. Phys.* **7**, 502–507 (2011).
34. Son, H., Park, J. J., Ketterle, W. & Jamison, A. O. Collisional cooling of ultracold molecules. *Nature* **580**, 197–200 (2020).
35. Ho, T.-L. Universal thermodynamics of degenerate quantum gases in the unitarity limit. *Phys. Rev. Lett.* **92**, 090402 (2004).
36. Eigen, C. et al. Universal prethermal dynamics of Bose gases quenched to unitarity. *Nature* **563**, 221–224 (2018).

Methods

Experimental procedure

The starting point of our experiment is a BEC of 6×10^4 caesium atoms prepared in a disk-shaped dipole trap with a radius of 18 μm in the x–y horizontal plane. The disk-shaped potential is provided by a digital micromirror device (DMD), which projects 788 nm blue-detuned laser light on the plane with 1 μm resolution. The atoms are loaded into a single layer of the optical lattice in the vertical direction with trap frequency $\omega_z/2\pi = 400$ Hz (ref. [37]) A magnetic field gradient of 31 G cm^{-1} is applied to levitate the atoms and the magnetic field is tuned to 20.03 G.

We create the molecules with the g-wave narrow Feshbach resonance located at 19.87 G based on a procedure similar to that in ref. [21]. Since atoms and molecules have different magnetic moments, they tend to separate vertically in the presence of a magnetic field gradient. To better confine both atoms and molecules in the molecular formation phase, we increase the magnetic field gradient to 41.9 G cm^{-1} in 2 ms before ramping the magnetic field to 19.79 G in 2 ms, which creates the molecules. After the formation of the molecules, the magnetic field gradient is increased to 50 G cm^{-1} in 0.5 ms, which levitates the molecules and overlevitates the atoms.

To remove residual atoms after the molecular formation phase, a resonant light pulse of 60 μs illuminates and pushes atoms away from the imaging area in 4 ms. Molecules are detected by reversely ramping the magnetic field, which dissociates the molecules back to atoms, and the atoms are detected by absorption imaging. The final value of the magnetic field and the hold time are selected to give a reliable image that reflects the distribution of the molecules. In our experiments, we set the final magnetic field to be 20.19 G and do the detection in 0.1 ms after the reverse ramp. We estimate that the atoms expand by 1 μm during the dissociation process, which is comparable with the imaging resolution of our experimental system.

Characterization of external potential from atomic density profile

The strong magnetic field gradient for levitating the molecules leads to an additional magnetic anti-trapping potential on the horizontal plane. We also apply a central potential barrier projected from a DMD to measure the density response of the molecules. A precise knowledge of both the magnetic anti-trapping potential and the optical potential barrier are needed in order to extract the equation of state of the molecular gas.

We load atomic BEC into the same trap as for molecules to calibrate the external potential. Since the magnetic moment and polarizability of the g-wave molecule are accurately known, the trapping potential for molecules can thus be obtained from the trapping potential for atoms.

The magnetic anti-trap frequency on the horizontal plane is given by

$$\omega_i^2 = \frac{\mu_m}{4mB_0}(B'^2 - 4\varepsilon_i B_0^2), \quad (1)$$

where $i = x, y$, μ_m is the magnetic moment, B_0 and B' are the magnetic field and the magnetic field gradient, respectively, at the location of the particles and ε_i is determined from the coil geometry[37]. We determine the offset field value B_0 with an accuracy of 2 mG using microwave spectroscopy. We prepare atomic BEC at 17.2 G where the s-wave scattering length is $a_S = 4a_0$. Because of the low chemical potential, the atomic density distribution is sensitive to the magnetic anti-trap and the density is lower at the centre and higher in the rim; see Extended Data Fig. 1a. Since the vertical trap frequency $\omega_z/2\pi = 400$ Hz is much larger than the chemical potential $\mu_0/h \approx 10$ Hz, the BEC is in the quasi-2D regime and the column density under the Thomas–Fermi approximation is given by

$$n(x,y) = \frac{m}{\hbar^2 g_{2D}}[\mu_0 - V_{mag}(x,y)], \quad (2)$$

where the 2D coupling strength is $g_{2D} = \sqrt{8\pi}a_S/l_z$, with the harmonic oscillator length given by $l_z = \sqrt{\hbar/m\omega_z}$, the magnetic anti-trap potential $V_{mag}(x,y)$ is parametrized by the trap frequencies ω_x and ω_y as $V_{mag}(x,y) = -m\omega_x^2(x-x_0)^2/2 - m\omega_y^2(y-y_0)^2/2$ and (x_0, y_0) is the centre position of the anti-trap. To determine the trap frequencies and the global chemical potential, we fit the in situ atomic density distribution using equation (2); see Extended Data Fig. 1a. From the fit we obtain $\omega_x/2\pi = 1.94(9)$ Hz, $\omega_y/2\pi = 2.24(9)$ Hz and $\mu_0 = h \times 9.19(7)$ Hz. In this way, we calibrate the geometric parameters to be $\varepsilon_x = 0.54(3)\text{cm}^{-2}$ and $\varepsilon_y = 0.45(3)$ cm^{-2}, which we use to calculate the anti-trap frequencies for molecules based on equation (1), and obtain $\omega_x^{mol}/2\pi = 3.35(4)$ Hz and $\omega_y^{mol}/2\pi = 3.48(4)$ Hz. As a consistency check, we plot out the atomic density n_A versus the local chemical potential $\mu = \mu_0 - V_{mag}(x,y)$, which agrees with the equation of state of a pure 2D BEC, $\mu = (\hbar^2 g_{2D}/m)n(x,y)$ (see Extended Data Fig. 1b).

We calibrate the optical potential barrier projected by DMD using atomic BEC prepared at 19.2 G, where the atomic scattering length is $a_S = 127a_0$ and the vertical trap frequency is $\omega_z/2\pi = 409$ Hz. The intensity of the optical barrier is ramped up within 10 ms. After waiting for another 2 ms, absorption imaging is performed in the vertical direction to record the atomic column density; see Extended Data Fig. 2a. Here the barrier height is controlled by the fraction of micromirrors f_{DMD} that are turned on. The fraction determines the intensity of the light projected onto the atom plane. In the region with higher light intensity, the atomic density is suppressed more, which in turn allows us to determine the light intensity. Because of the higher chemical potential of the BEC in this case, the density depletion has a larger dynamical range that helps us to calibrate a larger range of barrier height. Since the chemical potential is comparable to the vertical trap frequency, the BEC is in the 3D regime and the column density under Thomas–Fermi approximation is given by

$$n(x,y) = \alpha[\mu_0 - V_{opt}(x,y)]^{3/2} \quad (3)$$

where $\alpha = 4\sqrt{2}/(3g\sqrt{m}\omega_z)$, the 3D coupling strength $g = 4\pi\hbar^2 a_S/m$ and the local optical potential $V_{opt}(x,y)$ is proportional to the micromirror fraction as $V_{opt}(x,y) = p(x,y)f_{DMD}$. Thus for each pixel located at (x,y), we have $n^{2/3}(x,y) = \alpha^{2/3}[\mu_0 - p(x,y)f_{DMD}]$, from which the proportionality $p(x,y)$ can be extracted from a series of measurements with different f_{DMD}, see Extended Data Fig. 2b. Repeating the same procedure for all the pixels within the region of optical barrier, we can map out the spatial dependence of the proportionality $p(x,y)$, see Extended Data Fig. 2c. The polarizability of weakly bound molecules is approximately twice as large as that of a free atom, thus the corresponding proportionality for the molecules is $2p(x,y)$.

After calibrating both the magnetic potential $V_{mag}(x,y)$ and the optical potential $V_{opt}(x,y)$ for molecules, we can obtain the local molecular density as a function of the total external potential $V(x,y) = V_{mag}(x,y) + V_{opt}(x,y)$ and follow the fitting procedure in Methods section 'Fitting the equation of state for 2D and 3D Bose gases' to extract the global chemical potential μ_0. Then we obtain the corresponding local chemical potential μ and average the density over a certain spatial area with a proper range of local chemical potential to obtain the equation of state for molecules from the density profile and optical barrier measurements in Fig. 2. In addition, with knowledge of the optical potential profile, we obtain the equation of state for the BEC in the 3D regime; see the inset of Fig. 2c.

Density profiles of atomic and molecular BECs

Starting from a flat-topped atomic density profile, we prepare a molecular condensate in the 2D box trap after the magnetic field is ramped across the Feshbach resonance. It is clear that the molecules do not inherit the density profile from the atoms; see Fig. 2a and Extended Data Fig. 4. The molecular density profile depends sensitively on the curvature of the magnetic field and the optical barrier potential, which we introduce immediately after the ramp.

To understand the fast change of the molecular density profile, we note that there is a drastic difference between the interaction energy scale near the Feshbach resonance where the molecules are created and far away from the resonance where we observe the molecular BEC. On resonance, the interaction energy scale is $h \times 8{,}000$ Hz, determined by the 'Fermi energy'[35] in our system, and is also orders of magnitude higher than the molecular chemical potential of $h \times 61$ Hz measured far from the resonance. Thus, near the resonance the molecules can speedily form and establish equilibrium with the other particles. In Extended Data Fig. 3, it is clear that molecules are created from the atoms within 200 μs for various ramp speeds and that they develop the ring structure in their density profiles near the resonance.

Finally, after the formation of the molecules, the molecular density profile persists for a hold time of 15 ms or longer; see Extended Data Fig. 5. In the presence of the optical barrier potential, the central molecular density is suppressed to <25% of the peak density and the molecular lifetime is expected to be longer than 100 ms. In this case, we expect that the particle loss during the 10-ms ramp does not greatly influence the compressibility measurement.

Fitting the equation of state for 2D and 3D Bose gases

For a nondegenerate 2D ideal Bose gas, the phase space density is given by $n_\phi = -\ln(1-\zeta)$, where $\zeta = \exp(\beta\mu)$ is the fugacity, $\beta = 1/k_B T$ and $\mu = \mu_0 - V(x,y)$ is the local chemical potential. If the gas is interacting, a mean-field potential $2(\hbar^2 g_{2D}/2m)n(x,y)$ is added to the external potential, based on the Hartree–Fock approximation[28]. Then the equation of state for interacting 2D Bose gas becomes:

$$n(x,y) = -\frac{1}{\lambda_{dB}^2}\ln[1 - e^{\beta\mu - g_{2D} n(x,y)\lambda_{dB}^2/\pi}], \quad (4)$$

On the other hand, the density of 2D superfluid outside the fluctuation region is[27]:

$$n(x,y) = \frac{2\pi\beta}{g_{2D}\lambda_{dB}^2}\mu + \frac{1}{\lambda_{dB}^2}\ln[2n(x,y)\lambda_{dB}^2 g_{2D}/\pi - 2\beta\mu], \quad (5)$$

We apply the above models for a 2D Bose gas to describe the equation of state of the molecules, shown in Fig. 2c. We perform a global fit to the data points within the range $n_M < 1\ \mu m^{-2}$ and $n_M > 4\ \mu m^{-2}$ using equations (4) and (5), respectively, with temperature T, global chemical potential μ_0 and 2D coupling constant g_{2D} as fitting parameters. Since the experimental conditions drifted, the global chemical potential between the optical barrier and density profile measurements are different, and the chemical potential difference $\delta\mu$ is also set as an free parameter in the global fit. The fit gives $T = 11(1)$ nK, $g_{2D} = 0.19(3)$ and the global chemical potential for the optical barrier and density profile measurements as $h \times 45(7)$ Hz and $h \times 61(7)$ Hz, respectively. We also performed independent fits to the data at low-density $n_M < 1\ \mu m^{-2}$ and high-density $n_M > 4\ \mu m^{-2}$. The resulting temperatures are 10(3) nK and 11(1) nK, in agreement with each other and with the global fit.

With the extracted 2D coupling constant g_{2D}, the critical phase space density for the BKT superfluid transition is evaluated as $\ln(\xi/g_{2D}) \approx 7.5$, where the coefficient $\xi = 380(3)$ (ref. [27]). On the other hand, the BEC transition in our 2D box potential occurs at a critical phase space density of $\ln(4\pi R^2/\lambda_{dB}^2) \approx 7.5$ (ref. [28]), which coincides with the BKT transition.

For BECs in the 3D regime, as shown in the inset of Fig. 2c, the low-density part where the column density $n_A < 10\ \mu m^{-2}$ is fitted using the classical gas formula $n(x,y) = (2\pi l_z^2/\lambda_{dB}^4)\exp(\beta\mu)$. The high-density part is fitted based on equation (3).

Extraction of the two-body inelastic loss coefficients

To study the lifetime of g-wave molecules, we hold the molecules in different traps and monitor the decay of total particle number as a function of the hold time. The two traps we used have horizontal radii of $R_1 = 12.5$ μm and $R_2 = 9$ μm and vertical trap frequencies of $\omega_{z1}/2\pi = 400$ Hz and $\omega_{z2}/2\pi = 167$ Hz, respectively. The molecular density distributions in these traps are approximately uniform in the horizontal direction and Gaussian in the vertical direction, given by

$$n(\mathbf{r}) = \frac{N_M}{\pi^{3/2} R_i^2 l_{zi}} e^{-z^2/l_{zi}^2}\theta(R_i - \rho), \quad (6)$$

where $i = 1, 2$, $\rho = \sqrt{x^2 + y^2}$ and $\theta(x)$ is the Heaviside step function.

Even though the 1,064 nm light intensity in the vertical direction of the two traps differs by a factor of $\omega_{z1}^2/\omega_{z2}^2 \approx 6$, the decay rates of molecular numbers are similar; see Fig. 3a. This suggests that the one-body loss process due to the off-resonant laser light is negligible. In fact, since the g-wave molecules are in a highly excited rovibrational state, the two-body loss process dominates, which is modelled by $\partial_t n(\mathbf{r}, t) = -L_2 n^2(\mathbf{r}, t)$. The molecular number decay corresponding to the density profile in equation (6) is thus given by

$$N_M(t) = \frac{N_M(0)}{1 + L_2' N_M(0) t}, \quad (7)$$

where $L_2' = L_2/\sqrt{2}\pi^{3/2} R_i^2 l_{zi}$. We use equation (7) to fit the data of molecular number decay and extract the inelastic loss coefficient L_2 in Fig. 3b.

The unitarity limit of the two-body loss coefficient is $U_2(k) = 4h/2mk$, where k is the magnitude of the relative wavevector $\mathbf{k}$ between two colliding molecules, associated with the relative kinetic energy $E = \hbar^2\mathbf{k}^2/2m$ (ref. [16]). Owing to the finite temperature in our experiment, the relative kinetic energy obeys the Boltzmann distribution as $p(E) = A\exp(-E/k_B T)$, where the coefficient $A = (1/4)(\hbar^2/\pi m k_B T)^{3/2}$. The distribution of the wavenumber k is then given by

$$p(k) = 4\pi A k^2 e^{-\hbar^2 k^2/2mk_B T}. \quad (8)$$

The unitarity limit that we evaluate in Fig. 3b is $U_2 = \int_0^\infty U_2(k)p(k)\mathrm{d}k = (4h/2m)\langle k^{-1}\rangle$, where the thermal average of k^{-1} with respect to the distribution $p(k)$ is $\langle k^{-1}\rangle = \sqrt{\hbar^2/\pi m k_B T}$. For comparison with the loss coefficients, we evaluate the interaction scale as $\mu_0/\hbar n_{3D}$, where the 3D mean density is $n_{3D} = \int_{-\infty}^{+\infty} n^2(\mathbf{r})\mathrm{d}^3\mathbf{r}/\int_{-\infty}^{+\infty} n(\mathbf{r})\mathrm{d}^3\mathbf{r} = N_M/\sqrt{2}\pi^{3/2} R_1^2 l_{z1}$.

Empirical fits to dissociation rate and dissociated molecular fraction

After preparing a purely molecular BEC below the Feshbach resonance, if the magnetic field is then switched to a value high above the resonance, the molecules quickly dissociate into a continuum of free atoms. The dissociation rate follows Fermi's golden rule as $\Gamma = (2\pi/\hbar)|V_{MA}|^2\rho(E) = 2m^{1/2} a_{bg}\Delta\mu\Delta B E^{1/2}/\hbar^2$, where V_{MA} is the coupling matrix element between the molecular and atomic states and is independent of the energy E above the continuum to leading order, the density of state $\rho(E) \propto E^{1/2}$ and a_{bg} is the background scattering length. In this high-field limit, our measured dissociation rate is consistent with Fermi's golden rule $\gamma = \alpha\Gamma$, where the coefficient $\alpha = 0.4(1)$. The fact that α is less than 1 may be because the resonance width ΔB from the measurement of the Innsbruck group[22] we used in evaluating Γ is larger than the actual resonance width. The dissociation rate in Fig. 4b is extracted by fitting the data in Fig. 4a using the formula $N_M(t) = N_M(t_0)\{1 - \exp[-\gamma(t - t_0)]\}\theta(t - t_0)$, where t_0 is the time when the molecules start to dissociate.

On the other hand, when the magnetic field is ramped to near the resonance where $\rho(E) \approx 0$, we still observe a finite dissociation rate of 8 m s^{-1}. This is because the molecular state can couple to a band of scattering states that are Lorentzian distributed[38]. We thus define an effective density of state ρ_{eff} to be a convolution between $\rho(E)$ and a Lorentzian distribution. Thus the effective dissociation rate becomes

$$\Gamma_{eff} = \Gamma\sqrt{(\sqrt{1 + \Omega^2/4E^2} + 1)/2}, \quad (9)$$

where Ω is the full width of the Lorentzian distribution. We use equation (9) to fit the dissociation rate as a function of the magnetic field we measured, shown as the blue solid line in the upper panel of Fig. 4b.

The dissociated molecular fraction drops when the magnetic field is ramped back closer to the resonance, which we attribute to the inelastic collision loss between atoms and molecules near the resonance. The data of the fraction in Fig. 4b is fitted using a sigmoid function $f = 1/2 + (1/\pi)\arctan[\Delta\mu(B-B_0)/\delta]$, where δ is a free parameter.

Data availability

The data that support the plots within this paper and other findings of this study are available from the corresponding author upon reasonable request. Source data are provided with this paper.

Code availability

The codes for the analysis of data shown within this paper are available from the corresponding author upon reasonable request.

37. Hung, C.-L. In Situ Probing of Two-Dimensional Quantum Gases. http://pi.lib.uchicago.edu/1001/cat/bib/8855526 Thesis, Univ. Chicago (2011).
38. Fano, U. Effects of configuration interaction on intensities and phase shifts. *Phys. Rev.* **124**, 1866–1878 (1961).

Acknowledgements We thank P. Julienne for discussions and K. Patel for carefully reading the manuscript. This work is supported by National Science Foundation (NSF) grant number PHY-1511696, the Army Research Office Multidisciplinary Research Initiative under grant W911NF-14-1-0003 and the University of Chicago Materials Research Science and Engineering Center, which is funded by the NSF under grant number DMR-1420709.

Author contributions L.C. and Z.Z. designed and performed the experiments. Z.Z. analysed the data. All authors contributed to discussions on the experiment and preparation of the manuscript. C.C. supervised the project.

Competing interests The authors declare no competing interests.

Additional information
Supplementary information The online version contains supplementary material available at https://doi.org/10.1038/s41586-021-03443-0.
Correspondence and requests for materials should be addressed to C.C.
Peer review information *Nature* thanks the anonymous reviewers for their contribution to the peer review of this work. Peer reviewer reports are available.
Reprints and permissions information is available at http://www.nature.com/reprints.

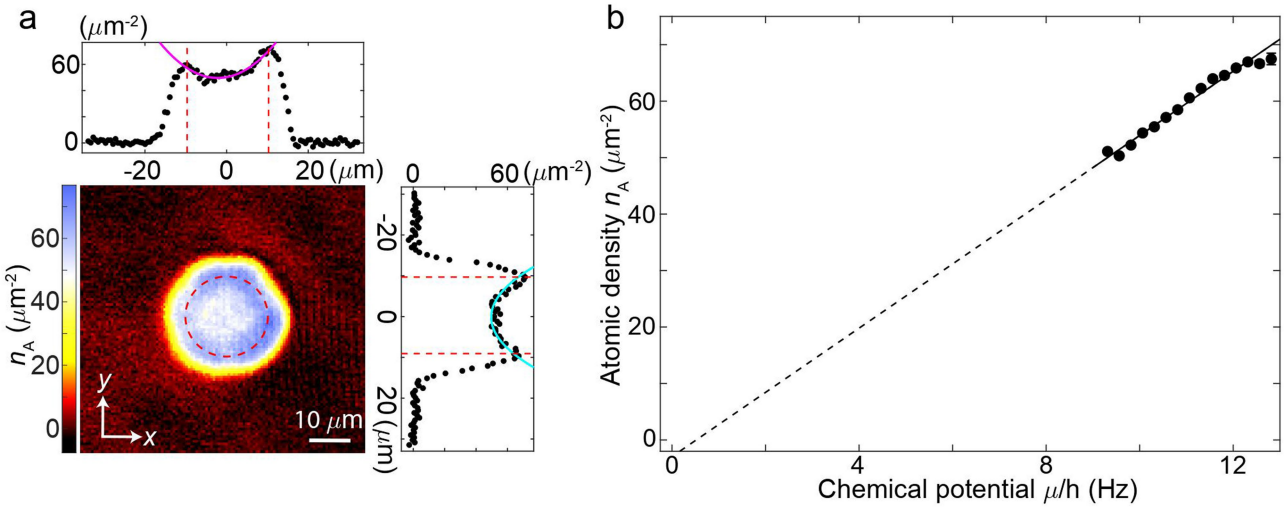

Extended Data Fig. 1 | Calibration of magnetic anti-trap potential from the atomic density distribution. a, Fit of the in situ atomic density profile for determination of the magnetic anti-trap frequencies ω_x and ω_y using equation (2). The top and right panels show line cuts of the 2D atomic density in the x and y directions, crossing at the centre of the anti-trap. We choose the region within the red dashed circle for fit and extraction of the equation of state. **b**, Equation of state of atomic BEC shown in **a**. Each data point represents averaged density within a bin size $\delta\mu/h = 0.25$ Hz and error bars represent one standard deviation. The black solid line is a linear fit to the data, while the black dashed line is an extrapolation of the fit towards the origin. Data values and error bars are estimated as in Fig. 2 from 20 measurements.

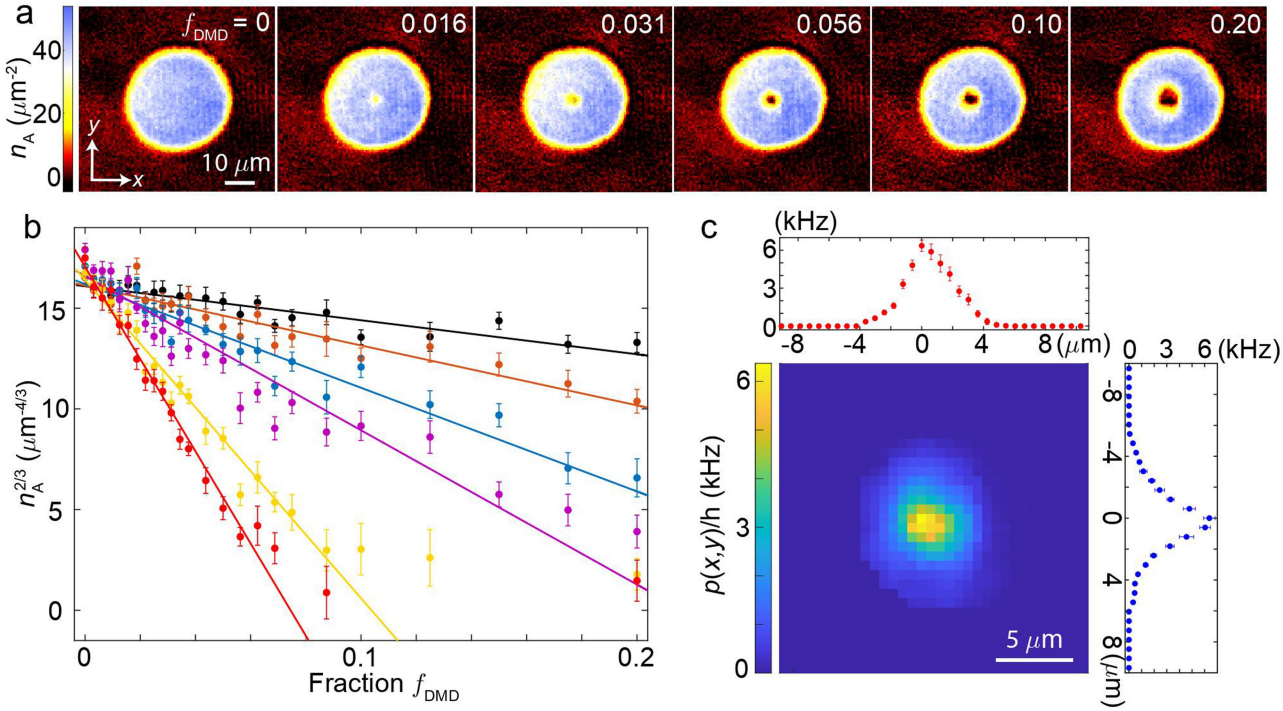

Extended Data Fig. 2 | Calibration of the optical potential barrier projected by a DMD from the density response measurement of atomic BEC. a, Images of in situ atomic column density with different central barrier heights determined by different fractions of micromirrors f_{DMD} that are turned on in the DMD. **b**, Example measurements of the proportionality $p(x, y)$ for six pixels at different locations. The solid lines are linear fits to the linear part of the data points, the slope of which gives $p(x, y)$. Data values and error bars are estimated as in Fig. 2 from 9–11 measurements. **c**, Spatial dependence of the proportionality $p(x, y)$. The upper and right panels are line cuts in the x and y directions crossing the peak value. Data values are determined from the fits and the errorbars represent 95% confidence interval.

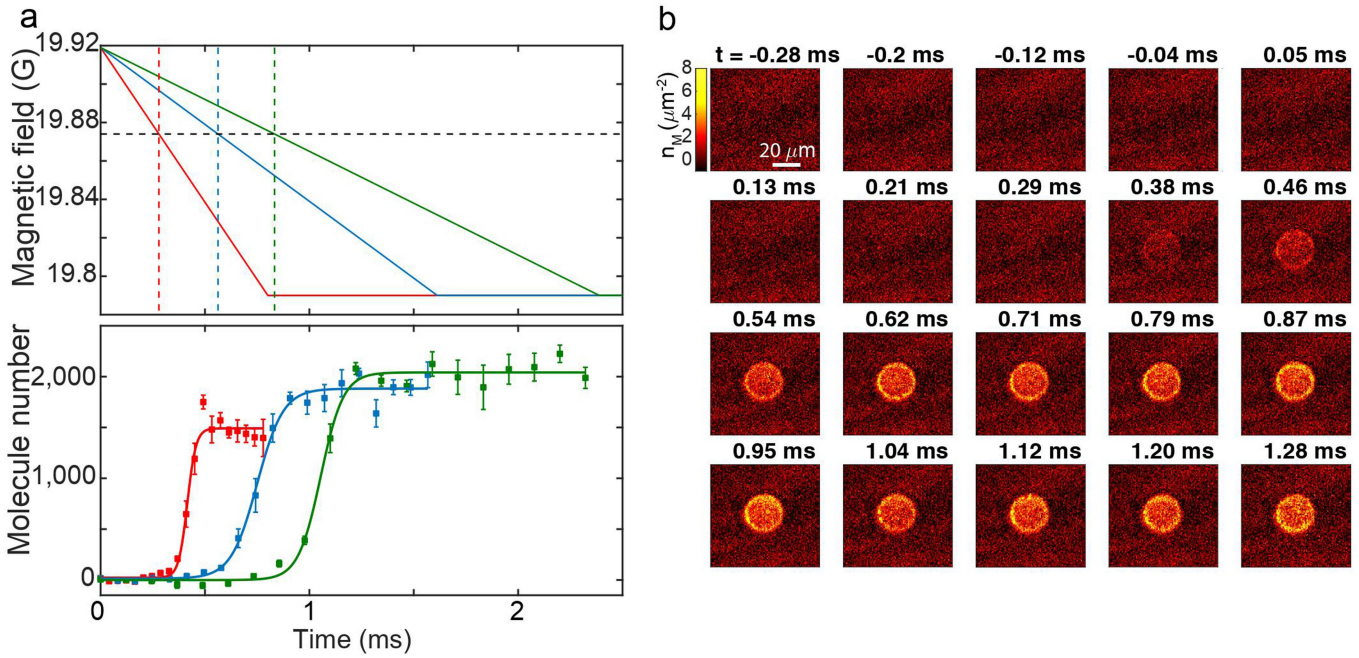

Extended Data Fig. 3 | Fast equilibration of molecules with atoms during the ramp across the Feshbach resonance. a, Dynamics of the number of molecules during the magnetic field ramp across the Feshbach resonance at 19.87 G with different ramp speeds of 161 mG ms^{-1} (red), 80 mG ms^{-1} (blue) and 54 mG ms^{-1} (green). **b**, In situ images of molecules during the magnetic field ramp at 80 mG ms^{-1}. Data values and error bars are estimated as in Fig. 2 from 5–7 measurements.

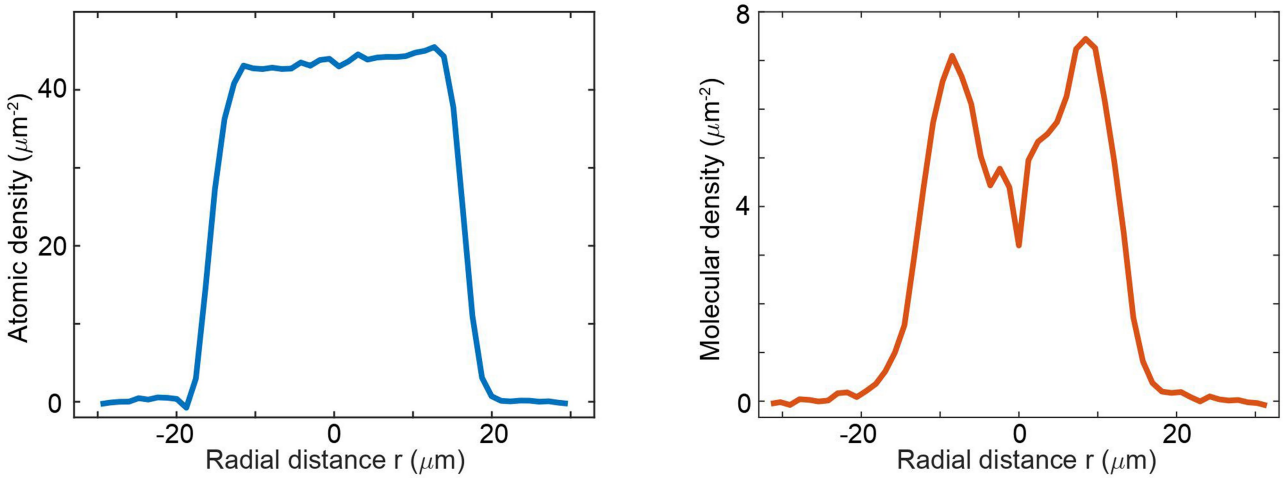

Extended Data Fig. 4 | Azimuthally averaged density profiles. These profiles correspond to the atomic (left) and molecular (right) clouds shown in Fig. 2a. The atomic density profile is flat-topped, whereas the molecular density profile has a dip in the middle.

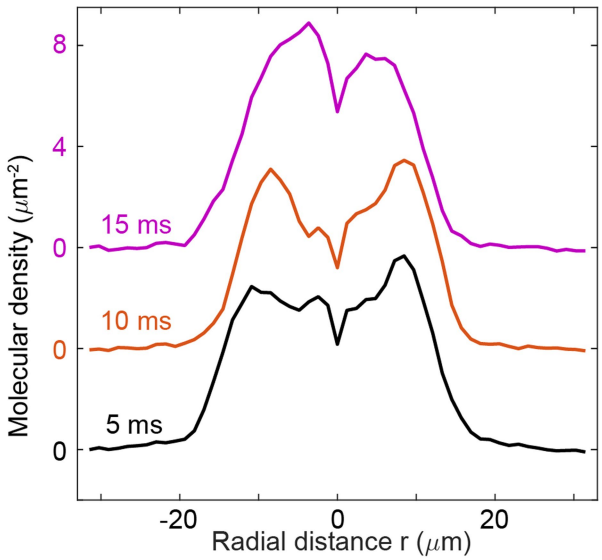

Extended Data Fig. 5 | Dynamics of molecular density profiles in the 2D box trap with magnetic anti-trap potential. The azimuthally averaged molecular density profiles are shown as a function of the hold time after the formation of molecules. The dips in the middle result from the magnetic anti-trap potential and persist during the first 15 ms after formation of the molecules.